Journal of Advanced Ceramics
2020, **9**(1): 55–63
https://doi.org/10.1007/s40145-019-0347-z
ISSN 2226-4108
CN 10-1154/TQ

Research Article

$NiWO_4$ powders prepared via polymeric precursor method for application as ceramic luminescent pigments

Naiara A. LIMA[a,*], Lorena D. S. ALENCAR[b], Máximo SIU-LI[a], Carlos A. C. FEITOSA[c], Alexandre MESQUITA[d], Jean-Claude M'PEKO[a], Maria I. B. BERNARDI[a]

[a]*Instituto de Física de São Carlos, Universidade de São Paulo, 13560-970 São Carlos, SP, Brazil*
[b]*Instituto Federal de Mato Grosso do Sul, IFMS, 79200-000 Aquidauana, MS, Brazil*
[c]*Departamento de Física, Centro de Ciências Exatas e Tecnologia, Universidade Federal do Maranhão, UFMA, 65080-805, São Luis, MA, Brazil*
[d]*Instituto de Geociências e Ciências Exatas, Departamento de Física, Universidade Estadual Paulista, 13506-900, Rio Claro, SP, Brazil*

Received: March 24, 2019; Revised: August 5, 2019; Accepted: August 13, 2019

Abstract: $NiWO_4$ was prepared using the polymeric precursor method and studied in terms of physical and chemical properties to verify its stability for industrial applications as pigments. The characterization was accomplished using thermal analyses, X-ray diffraction (XRD), scanning electron microscopy (SEM), photoluminescence (PL) and UV–Vis spectroscopies, colorimetric coordinates, and Raman spectra. Increasing the temperature, successive exothermic reactions were observed and they are related with thermal decomposition of the organic compound. The stability was reached at ~700 ℃. The material is verified to become completely free of second phase at ~800 ℃. The end $NiWO_4$ powders showed an intense charge transfer (CT)-related tail centered in the ultraviolet region, resulting in a yellow product. In addition, the powders exhibited broad excitation band and broad deep blue–green emission band, which were enhanced with increasing powders' crystallinity.

Keywords: nickel tungstate; yellow pigment; colorimetric coordinate; optical property; structural characterization

1 Introduction

Organic and inorganic materials have been largely used as yellow pigments, such as gamboge which is a pigment derived from a tree, the $Fe_2O_3{\cdot}H_2O$, which is found in clays, lead antimonate, zinc chromate, CdS, $PbCrO_4$, $NiOSb_2O_5{\cdot}20TiO_2$, and As_2S_3. However, these pigments have some characteristics that make them not ideal for use, such as toxicity, chemical, and thermal instability.

Due to the superior acid–alkaline, chemical and thermal stability, and coverage power of these materials [1], inorganic pigments are known to present several applications in the manufacture of porcelains, ceramic tiles, enamels, paints, rubber, imitation leather, varnishes, building materials, glass, glazes, and floor covering. However, many inorganic pigments with brilliant color and good functionality are contaminating products to be avoided because of their negative effect on environment

* Corresponding author.
E-mail: naiaraarantes@usp.br

and human health. With regard to yellow inorganic pigments, chromates of alkaline-earth metal ions (e.g., calcium, strontium, and barium), Naples yellow (lead antimonite), litharge (lead oxide), and yellow cadmium (cadmium sulfide) were for long time of particular importance due to their specific coloration, which was the reason of their wide use in ceramic tiles [1]. However, the use of these pigments is restricted in terms of commercial applications because of the toxicity of Cr, Cd, Sb, and Pb atoms [2–5]. Consequently, development of sustainable and environmentally friendly inorganic pigments and/or reducing the toxicity of existing inorganic pigments are two approaches strongly required.

Tungstates of formula AWO_4 ($A = Ni^{2+}$, Ca^{2+}, Sr^{2+}, Ba^{2+}) belong to an important family of functional inorganic materials [6,7] that have attracted great attention in the industry because of their interesting physical and chemical properties [8,9], mainly because they are not toxic. The divalent cations are called network modifiers and the tungsten atoms are called network formers. They can form two distinct structures depending on the ionic radius or cations. When the radius is greater than or equals to 0.99 angstroms, it allows the formation of the Scheelite structure (Ca^{2+}, Sr^{2+}, Ba^{2+}) and for radius smaller than 0.77 angstroms, the Wolframite structure is formed, which is the case of $NiWO_4$ [10–12]. From a technological viewpoint, the versatility of these materials in terms of possible applications includes: light emitting diodes (LEDs) [8], electrodes [12], cathode material for supercapacitors [13], photoluminescent materials [14], and photocatalyst [15,16]. In particular, nickel tungstate, the material targeted in this study, is one of the potential candidates to be used as yellow inorganic luminescent pigment [17].

Luminescent materials have the characteristic of emitting light when stimulated by chemicals and ionizing radiation. The luminescent pigments have several applications, among them, they are used in plates and transit lanes, markings on money notes, and in fabrics and wall paintings for decoration [14]. It should be pointed out that scientific and technological interest on these materials also arises because of dealing with low-cost and no polluting materials, that can be included in the group of sustainable products.

The chemical and physical properties of metal oxides, including tungsten oxides, depend on the synthetic route employed. There are two ways of synthesizing ceramic pigments: by chemical method such as co-precipitation [18–20], hydrothermal [21–23], and polymeric precursor method [24] or by solid-state reaction method. Among them, chemical methods, particularly the polymeric precursor method, show several advantages, such as homogeneous mixture of the reactants, purity, low cost, simple synthesis, temperatures below 800 ℃, and short time processing [25].

Therefore, the present work involved the synthesis of $NiWO_4$ nanoparticles achieved by applying the polymeric precursor method, which is a low-cost processing procedure, when compared to other chemical methods, besides ensuring high material reproducibility. The method has been successfully used in the synthesis of nanoparticles of different oxides [26], and is based on the chelation of cations by a hydrocarboxylic acid (normally citric acid), followed by polyesterification using a glycol (normally ethylene glycol) [27]. The formed precursor resins contain cations randomly distributed throughout the polymer [28,29]. The synthesized nickel tungstate powders were subsequently characterized by thermal analyses: thermogravimetric (TG), differential scanning calorimetry (DSC), X-ray diffraction (XRD), diffuse reflectance, colorimetric coordinate, scanning electron microscope (SEM), and Raman and photoluminescence (PL) spectroscopies.

2 Experimental

The processing of materials involved the dissolution of nickel nitrate in milli-Q water and the dissolution of tungstic acid in milli-Q water at 90 ℃ with a pH of 11. For the pH of tungstic acid solution reaches the value of 11, it is necessary to add ammonium hydroxide. On the other hand, citric acid was dissolved in milli-Q water. Both intermediary products were mixed so as to produce a tungsten citrate solution. The polymeric resin was synthesized by adding nickel nitrate to this solution under constant stirring and at a temperature of 120 ℃. Addition of ethylene glycol promoted the polyesterification reaction. The citric acid:metal molar ratio was 3:1; while the citric acid:ethylene glycol mass ratio was 2:3.

The polymeric precursor solution was heat treated at 400 ℃ for 4 h at a heating rate of 10 ℃·min^{-1}. The obtained powders were grounded in an agate mortar in order to deagglomerate the powders, and hereafter called the precursor powders which were treated at temperatures of 500–800 ℃ for 2 h, with a heating rate of 10 ℃·min^{-1}.

The material was characterized by thermal decomposition, XRD, UV–Vis spectroscopy, colorimetric coordinates, SEM, and Raman and PL spectroscopies. The thermal decomposition and crystallization of the

powders were studied by TG (Netzsch STA 409C) and DSC techniques under oxygen atmosphere at a heating rate of 10 ℃·min^{-1}. Al_2O_3 was used as reference material during the thermal analyses. Based on the results from the thermal analyses, as later presented, we considered heat-treating the precursor powders at 500–800 ℃ for 2 h to get a close insight into phase development. These heat treatments were performed in an electric furnace under air atmosphere, at a heating rate of 10 ℃·min^{-1}.

In the following, the samples were characterized by XRD at room temperature, towards the 2θ ranged from 20° to 80°, with a step of 0.020°, a scanning speed of 2 (°)·min^{-1}, and using Cu Kα radiation (Rigaku, ULTIMA IV).

The samples were also subjected to UV–Vis characterization (Shimadzu-UV-1601 PC spectrophotometer), and the spectra were measured in the range of 220–900 nm.

Colorimetric coordinates of the pigments were measured in the range of 300–700 nm, using a spectrophotometer (Minolta, CM2600d) equipped with a standard type D65 (day light) light source, and following the CIE-L*a*b* colorimetric method recommended by the Commission Internationale de l'Eclairage (CIE) [30]. In this method, L^* is the lightness axis (black (0)→white (100)), b^* is the blue (–)→yellow (+) axis, and a^* is the green (–)→red (+) axis, while ΔE is defined as the total color difference ($\Delta E^2 = L^{*2} + a^{*2} + b^{*2}$).

Microstructural characterization of the powders was carried out using a high resolution SEM (FEG–SEM Supra 35, Zeiss, Germany) operating at 3 kV.

Raman spectra were measured with a MonoVista CRS Raman spectrometer from Spectroscopy and Imaging GmbH. The samples were irradiated with a laser beam focused with an Olympus microscope. For the excitation in backscattering geometry, the 633 nm line of a He–Ne laser with 35 mW was used. PL spectra were collected with a Thermal Jarrel–Ash Monospec monochromator and a Hamamatsu R955 photomultiplier. The 350.7 nm exciting wavelength of a krypton ion laser (Coherent Innova 200) was used; the output of the laser was maintained at 500 mW, with ~14 mW.

3 Results and discussion

3.1 Thermal analyses

Figure 1 presents the TG, derivative thermogravimetry (DTG), and DSC curves of the $NiWO_4$ amorphous precursor powders. The TG curves reveal a series of mass loss-related decomposition reactions, connected to different exothermic events as indicating the DSC curves.

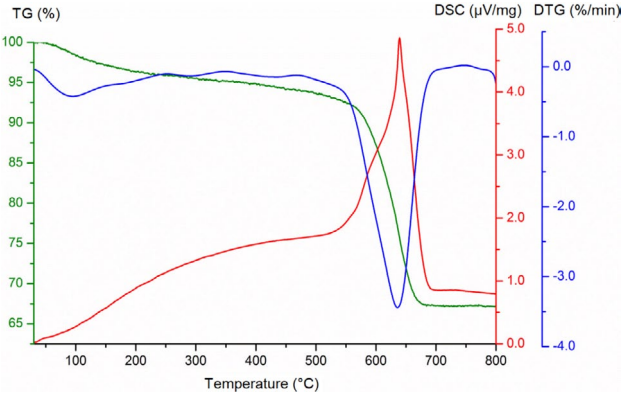

Fig. 1 TG, DTG, and DSC curves of the $NiWO_4$ precursor powder.

Development of these decomposition processes should be described considering the complexation of nickel with citric acid leading to the following reaction, noting formation of nitric acid and water as products.

$$Ni(NO_3)_2{\cdot}6H_2O + 2C_6H_8O_7 \rightarrow Ni(C_6H_7O_7)_2 + 2HNO_3 + 6H_2O \quad (1)$$

Meanwhile, the tungsten complexation reactions occur as follows, forming ammonium hydroxide.

$$H_2WO_{4(aq.)} \rightarrow WO_3 + H_2O \quad (2)$$

$$WO_3 + H_2O + 2NH_4OH \rightarrow W^{2+} + 2NH_4^+ + 2OH^- + O_2(g) \quad (3)$$

$$W^{2+} + 2NH_4^+ + 2OH^- + 2C_6H_8O_7 \rightarrow W(C_6H_7O_7)_2 + 2H^+ + 2NH_4^+ + 2OH^- \quad (4)$$

Mixing these metallic complexes (metallic citrates) above 70 ℃ triggers the onset of the esterification reaction between metal citrate and ethylene glycol, as follows:

$$M^{n+}[OCOCH_2C(OH)(COOH)CH_2COOH]_x + 3HOCH_2CH_2OH \rightarrow M^{n+}[OCOCH_2C(OH)(COOH)CH_2COOCH_2CH_2OH]_x + xH_2O \quad (5)$$

For the $NiWO_4$ compound studied here, the polyesterification reaction occurs continuously until the polymer network is formed. This network is expected to consist of the following basic units:

$$\{W^{4+}[OCOCH_2C(OCH_2{-}\ldots)(COOCH_2{-}\ldots)CH_2COOCH_2{-}\ldots]_4\}$$
$$\{Ni^{2+}[OCOCH_2C(OCH_2{-}\ldots)(COOCH_2{-}\ldots)CH_2COOCH_2{-}\ldots]_2\} \quad (6)$$

Accordingly, the main organic compounds contained in the resin are water, ammonium hydroxide, nitric acid, and polyester. During heat treatment of the $NiWO_4$ precursor powders, total elimination of these compounds traduces into a mass loss of about 33% accomplished when approaching 700 ℃, as reveals the TG curve in Fig. 1. In terms of details, three thermal superposed events are visible in the TG curve. The first region occurs in the temperature range of 50 to 169 ℃ and accounts for a mass loss of around 2.6%, attributed to the elimination of adsorbed H_2O. The second region involves a mass loss of 5.3% from 169 to 562 ℃, and this is related to dehydration of the resin, which becomes anhydrous due to the break of weakly bonded CH_2 groups. Finally, the third region goes from 562 to 672 ℃, and it involves a mass loss of 24.4%, attributed to the elimination of C–O groups as well as strongly bonded carbon atoms from the M–O–C groups, forming CO/CO_2.

Regarding the DSC curve, the elimination of water and decomposition of the organic compounds were also detected, all manifesting as exothermic events, followed by crystallization immediately taking place with a further increase of temperature. The highest crystallization peak occurs at ~639 ℃. Table 1 summarizes the thermal events and corresponding temperature ranges, as inferred from the TG and DSC data.

3. 2 Structural analysis

Crystallization and phase development were accompanied by XRD technique. The data are shown in Fig. 2.

It is observed that, after heat treatment at 500 ℃/2 h, the $NiWO_4$ precursor powders still reveal amorphous, while heat treatment at 600 ℃/2 h shows that formation of the crystalline phase has already occurred, but with traces of WO_3, as also reported by Quintana-Melgoza *et al.* [31]. Annealing the powders at 700 and 800 ℃/2 h allows synthesizing $NiWO_4$ powders without spurious phases, in good agreement with observation of a huge DSC peak at ~639 ℃ (Fig. 1) from the thermal analysis measurements conducted in dynamic mode (10 ℃·min^{-1}). This peak is asymmetric towards lower temperatures, suggesting to involve an overlap with a low-intensity one, most likely related to synthesis of the above-mentioned WO_3 phase when approaching 600 ℃ (Fig. 2). In particular, the $NiWO_4$ was indexed in the wolframite monoclinic structure (space group: $P2/c$, with $Z = 2$), characterized by alternating layers of transition-metal and tungsten atoms parallel to the (100) plane. This is a structure where the oxygen atoms are hexagonally closely packed, and the metal ions occupy a quarter of all the octahedral sites [32]. The crystallite size (D_c) in the $NiWO_4$ powders was estimated from the XRD data by using the Scherrer equation:

$$D_c = K\lambda/\beta\cos\theta \quad (1)$$

where K is a shape factor and usually is ~0.9, λ is the wavelength of X-ray source that used in XRD measurements, β is the breadth of the observed diffraction line at its half intensity maximum, and θ is the corresponding angle. The results are 43 and 47 nm after heat treatments at 700 and 800 ℃, respectively.

Table 1 Results of thermal analyses for the $NiWO_4$ sample

Temperature range from TG (℃)	Weight loss (%) from TG	Thermal event details
50–169	2.6	H_2O and adsorbed gas elimination
169–562	5.3	Polymeric degradation (–CH_2– groups)
562–672	24.4	Polymeric degradation (–CO– and –COO– groups)
> 672	—	Decomposition of the organic compounds accomplished

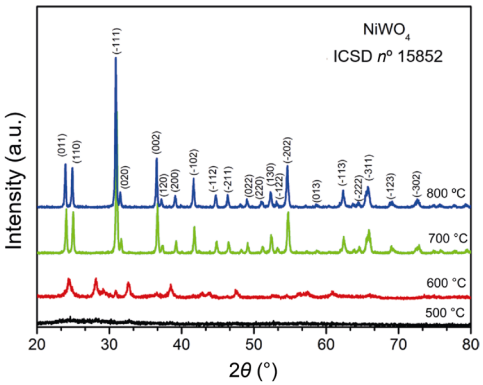

Fig. 2 XRD patterns of $NiWO_4$ powders after annealing at 500, 600, 700, and 800 ℃ for 2 h.

3. 3 UV–Vis spectra

Figure 3 shows the UV–Vis spectra performed in the diffuse reflectance mode of the $NiWO_4$ powders annealed at 500 up to 800 ℃/2 h. The pictures of each sample are also presented. As can be seen in Fig. 3 and XRD results, $NiWO_4$ sample annealed at 500 ℃ is a black powder in which the material is amorphous, explaining the spectra observed. As the temperature increases, the $NiWO_4$ powders crystallize and become

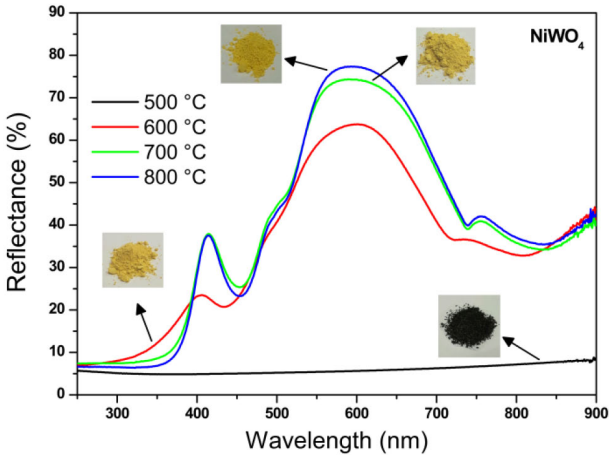

Fig. 3 Reflectance spectra of $NiWO_4$ samples calcined at 500–800 ℃/2 h.

yellow. The reflectance spectra of the samples annealed at 600, 700, and 800 ℃ show broad peak centered in the yellow and a low peak in blue region of the spectra.

Qualitative and quantitative information about the color of the samples are shown in Table 2 which presents the colorimetric coordinates (L^*, a^*, and b^*) of the $NiWO_4$ stable samples calcined at 700 and 800 ℃/2 h.

The data were collected using light source type D65-10° (day light) and analyzed following the CIE-L*a*b* standard colorimetric method. Figure 4 shows the CIELab graphics of such $NiWO_4$ samples.

Table 2 Colorimetric coordinates (L^*, a^*, and b^*) of $NiWO_4$ samples calcined at 700 and 800 ℃/2 h, using light source type D65-10° (day light), following the CIE-L*a*b* standard colorimetric method

Sample	L^*	a^*	b^*
Standard (A)	99.45	–0.09	–0.04
Ni700 (D)	85.31	3.07	38.32
Ni800 (E)	85.36	4.93	42.95

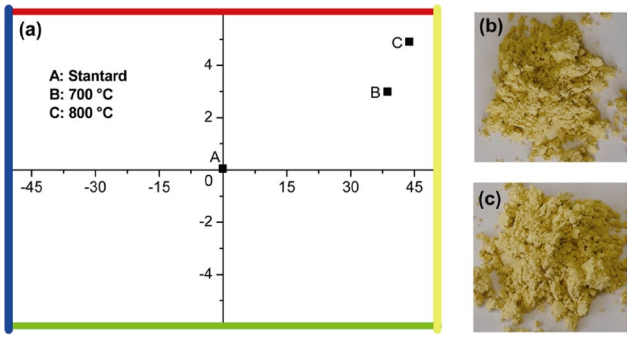

Fig. 4 (a) CIELab graphics of the $NiWO_4$ samples calcined at 700 and 800 ℃/2 h. Pictures of samples calcined at (b) 700 and (c) 800 ℃/2 h.

The color of Ni^{2+}-based compounds is directly influenced by the symmetry of its site [33]. The degeneracy of the $^3T_{1g}$, $^3T_{2g}$, and ^3E_g states of Ni^{2+} in octahedral geometry is lifted, and multiple-absorption bands occur when Ni^{2+} is situated in a coordination environment of low symmetry. Bands split by low symmetry will show peak wavelengths, which are polarization dependent [33]. Bright yellow color results when Ni^{2+} is in a deltahedric-coordinated site significantly distorted from the octahedral symmetry. Increased absorption intensity occurs when the metal ion *d–d* bands are in proximity to an ultraviolet charge transfer (CT) band.

Calculated from reflectance, the absorbance spectra of these powders were also processed, the behavior of which revealed qualitatively similar from sample to sample. The results allowed to estimate band gaps according to Ref. [10]:

$$\alpha h\nu = B(h\nu - E_g)^n \quad (2)$$

where α is the absorption coefficient of the material (calculated from the absorption spectra), h is the Plank's constant, ν is the frequency of the radiation, B is a constant (dependent on the nature of the material), and E_g is the energy of the band gap. n is a coefficient dependent on the type of transition considered: $n = 1/2$ for allowed direct transitions, while $n = 2$ for allowed indirect transitions.

Figure 5 depicts the absorbance spectra for $NiWO_4$ annealed at 700 and 800 ℃. In summary, absorbance bands at 1.55, 1.72, 2.85, and 3.95 eV applied for the sample heat treated at 600 ℃, resulting slightly shifted to 1.48, 1.68, 2.73, and 3.84 eV for the samples heat treated at 700 and 800 ℃. All these values are very close to those found by de Oliveira *et al.* [34]. We note that the first two bands of low intensity are localized in the blue region, while the third and fourth ones with higher intensity lie in the ultraviolet region. As indicated in Fig. 5, these bands have been proposed to arise from presence of Ni^{2+} and CT between clusters [34]. In particular, the bands at 1.68 and 2.73 eV would originate from the forbidden electronic transitions from $3A_{2g}$ to $1E_g$ and $1T_{2g}$, respectively, while the last band at 3.84 eV would involve CT transitions. In addition, Cimino *et al.* [35] reported that $Ni^{2+}O_4$ presents a $3T_1 \rightarrow 1T_2$ transition at 1.56–1.60 eV. Based on this information, we believe that the band at 1.48 eV should be assigned to the presence of $Ni^{2+}O_4$, indicating that Frenkel defects are present in $NiWO_4$ with the dislocation of Ni^{2+} from octahedral to tetrahedral sites [34].

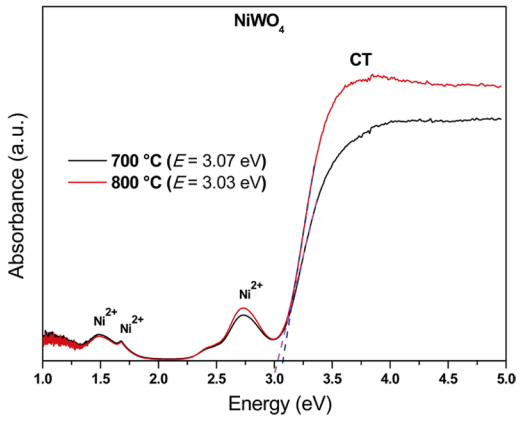

Fig. 5 Absorbance spectra of the $NiWO_4$ annealing at 700 and 800 ℃/2 h.

3.4 Field emitting gun–scanning electron microscopy (FEG–SEM) analysis

Figure 6 shows representative FEG–SEM micrograph from the powders heat treated at 700 ℃/2 h. This reveals to be here dealing with spherical-like packed particles, each with an average size of ~90 nm. This value is about twice the crystallite size estimated by XRD. For application as ceramic pigments, it is known that using nanoparticles is advantageous in order to produce more uniform and intense colors because of the huge surface area when compared to micrometer-sized particles [36].

3. 5 Raman analysis

According to group theory calculations, tungstates with triclinic or monoclinic structures exhibit 36 different Raman vibrational modes, 18 of which are expected to be active modes ($8A_g+10B_g$). Figure 7 is an example of the Raman data collected for the $NiWO_4$ powders heat treated at 700 and 800 ℃/2 h and Table 3 shows a

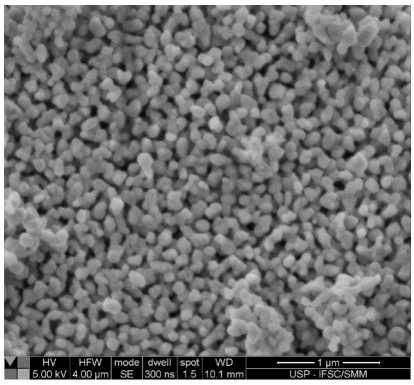

Fig. 6 SEM morphology of the $NiWO_4$ powders calcined at 700 ℃/2 h.

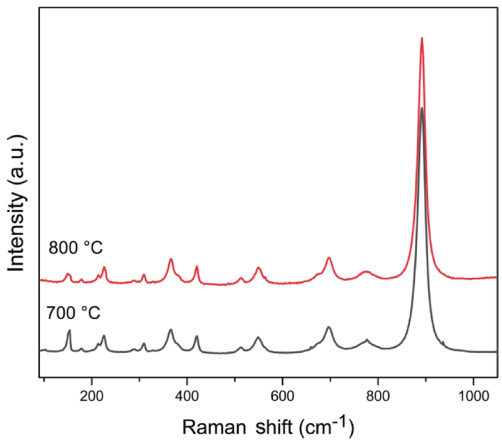

Fig. 7 Raman spectra of the $NiWO_4$ powders calcined at 700 and 800 ℃ for 2 h.

Table 3 $NiWO_4$ vibration modes

v (cm^{-1}) [8]	Phonon symmetry	700 ℃	800 ℃
97	B_g	102	—
149	A_g	151	152
174	B_g	178	177
197	B_g	199	201
210	B_g	213	214
223	A_g	225	225
287	A_g	288	288
307	A_g	308	309
326	B_g	327	328
363	A_g	365	365
380	B_g	378	379
418	A_g	419	419
512	B_g	512	513
549	A_g	548	549
675	B_g	673	673
697	A_g	696	696
775	B_g	776	774
893	A_g	891	890

comparison of the vibrational modes and the results found from Ref. [8]. Actually, 18 active Raman modes were observed, in total agreement with the results reported by Ross-Medgaarden and Wachs [37]. In general, according to Ref. [38], vibrational modes observed in the Raman spectra of tungstates may be classified into two groups, namely, external (< 600 cm^{-1}) and internal (> 600 cm^{-1}) modes [37]. The vibrational external modes are related to a lattice phonon, which involves

the motion of distorted octahedral [NiO_6] clusters with symmetry and rigid cell units. Meanwhile, vibrational internal modes are related to the vibration of the distorted octahedral [WO_6] clusters in the lattice, assuming that the center of mass is in a stationary state. Still according to Ross-Medgaarden and Wachs [37], the position of the most intense band, located at 891 cm^{-1} in Fig. 7, is associated with the WO_6 symmetric stretching vibration.

Therefore the characteristic vibrational modes which are shown in the Raman spectrum confirm the presence of a single phase, in agreement with the results of the XRD measurement.

3.6 PL studies

Figure 8 illustrates the PL spectra for the $NiWO_4$ samples annealed at 500–800 ℃/2 h, collected towards the 350–850 nm wavelength range, using 290 nm as excitation wavelength. PL spectra are a fingerprint of electronic transitions associated with the intrinsic emission occurring, here, within the wolframite structure. The $NiWO_4$ powders showed a broad deep blue–green emission band, which was enhanced with increasing crystallinity of the powders. These patterns are similar to those observed in other wolframite compounds [39], in which the emission bands were argued to arise from the WO_6^{6-} complex, along with defects in the crystal structure. Previous studies [40,41] proposed that blue and green emissions may be due to the intrinsic WO_6^{6-} complex with a double emission from one and the same center ($^3T_{1u}$–$^1A_{1g}$), while the yellow emission results from recombination of electron–hole pairs localized at oxygen atom-deficient tungstate ions. There is an additional suggestion from Refs. [39,42], according to which self-trapped excision in tungstate crystals with strong electron–phonon coupling may account for the blue band, and the transitions of T_{2u}–T_{2g} and T_{1g}–T_{2g} in the WO_6^{6-} complex could be responsible for the observation of green and yellow bands.

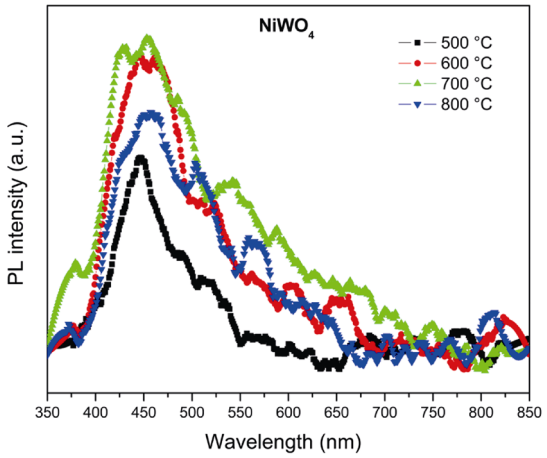

Fig. 8 PL emission spectra at room temperature from the $NiWO_4$ powders calcined at 500–800 ℃ for 2 h.

As can be seen in Fig. 8 that the $NiWO_4$ emission in the visible range between 350 and 700 nm, it can absorb all light from the visible spectrum, which makes it a good material for luminescent applications as in banners and road signs, for example, using white light that contains all the colors of the visible spectrum. Another observation is that for samples calcined at 600, 700, and 800 ℃, they have a higher intensity of light emission and are more visible when they are illuminated.

4 Conclusions

$NiWO_4$ nanopowders were successfully obtained by the polymeric precursor method after annealing at 700 ℃/2 h. The $NiWO_4$ was indexed in the wolframite monoclinic structure (space group: $P2/c$, with $Z = 2$), noting that increasing the calcination temperature also led to an increase in structural ordering. Bright yellow nickel compounds occur as a consequence of nickel entering in deltaedric-coordinated sites, representing a significant distortion of the octahedral geometry. The color is a result of electronic transitions related with Ni^{2+}. In addition, 18 active Raman modes were identified for $NiWO_4$ powders heat treated at 700 and 800 ℃. The $NiWO_4$ powders showed a broad deep blue–green emission band, and calcined samples of 600 to 800 ℃ are the most capable of emitting light when illuminated by white light. Overall, the results show that $NiWO_4$ may be a promising material for industrial application as luminescent pigments. Advantages of this material include the fact that it is a non-toxic inorganic material with good chemical stability and reproducibility, as compared to organic compounds.

Acknowledgements

The authors gratefully acknowledge the financial support from Brazilian research funding agencies, namely, FAPESP (Grant Nos. 2013/07909-4 and 2013/07296-2), CAPES, and CNPq (Grant No. 470069/2013-9).

References

[1] He XM, Wang F, Liu H, *et al*. Synthesis and coloration of highly dispersed $NiTiO_3$@TiO_2 yellow pigments with core-shell structure. *J Eur Ceram Soc* 2017, **37**: 2965–2972.

[2] Wanrooij PHP, Agarwal US, Meuldijk J, *et al*. Extraction of CdS pigment from waste polyethylene. *J Appl Polym Sci* 2006, **100**: 1024–1031.

[3] Bae B, Wendusu, Tamura S, *et al*. Novel environmentally friendly inorganic yellow pigments based on gehlenite-type structure. *Ceram Int* 2016, **42**: 15104–15106.

[4] Kawasaki T, Kono K, Dote T, *et al*. Markers of cadmium exposure in workers in a cadmium pigment factory after changes in the exposure conditions. *Toxicol Ind Health* 2004, **20**: 51–56.

[5] Jansen M, Letschert HP. Inorganic yellow-red pigments without toxic metals. *Nature* 2000, **404**: 980–982.

[6] Zhou YX, Yao HB, Zhang Q, *et al*. Hierarchical $FeWO_4$ Microcrystals: Solvothermal synthesis and their photocatalytic and magnetic properties. *Inorg Chem* 2009, **48**: 1082–1090.

[7] Hitha H, Jose A, Varghese T. Synthesis, characterization and photocatalytic activity of $NiWO_4$ nanoparticles. *AIP Conf Proc* 2019, **2082**: 030017.

[8] Harshan H, Priyanka KP, Sreedevi A, *et al*. Structural, optical and magnetic properties of nanophase $NiWO_4$ for potential applications. *Eur Phys J B* 2018, **91**: 287.

[9] Du XQ, Shao QZ, Zhang XS. Metal tungstate dominated $NiCo_2O_4$@$NiWO_4$ nanorods arrays as an efficient electrocatalyst for water splitting. *Int J Hydrog Energy* 2019, **44**: 2883–2888.

[10] Babu ES, Rani BJ, Ravi G, *et al*. Novel $NiWO_4$ nanoberries morphology effect on photoelectrochemical properties. *Mater Lett* 2018, **220**: 209–212.

[11] Ryu JH, Yoon JW, Lim CS, *et al*. Microwave-assisted synthesis of nanocrystalline MWO_4 (M: Ca, Ni) via water-based citrate complex precursor. *Ceram Int* 2005, **31**: 883–888.

[12] Huang YX, Yan C, Shi X, *et al*. $Ni_{0.85}Co_{0.15}WO_4$ nanosheet electrodes for supercapacitors with excellent electrical conductivity and capacitive performance. *Nano Energy* 2018, **48**: 430–440.

[13] Tian JJ, Xue Y, Yu XP, *et al*. Solvothermal synthesis of $NiWO_4$ nanostructure and its application as a cathode material for asymmetric supercapacitors. *RSC Adv* 2018, **8**: 41740–41748.

[14] Becidyan AN. Luminescent pigments in security applications. *Color Res Appl* 1995, **20**: 124–130.

[15] Pourmortazavi SM, Rahimi-Nasrabadi M, Karimi MS, *et al*. Evaluation of photocatalytic and supercapacitor potential of nickel tungstate nanoparticles synthesized by electrochemical method. *New J Chem* 2018, **42**: 19934–19944.

[16] Dhand C, Dwivedi N, Loh XJ, *et al*. Methods and strategies for the synthesis of diverse nanoparticles and their applications: A comprehensive overview. *RSC Adv* 2015, **5**: 105003–105037.

[17] Blovská V, Bělina P, Šulcová P. Synthesis of tungstate pigments of the formula $MNd_2W_2O_{10}$ (M = Ni, Zn, Mn). *J Therm Anal Calorim* 2013, **113**: 83–89.

[18] García-Pérez UM, Martínez-de la Cruz A, Peral J. Transition metal tungstates synthesized by co-precipitation method: Basic photocatalytic properties. *Electrochimica Acta* 2012, **81**: 227–232.

[19] Montini T, Gombac V, Hameed A, *et al*. Synthesis, characterization and photocatalytic performance of transition metal tungstates. *Chem Phys Lett* 2010, **498**: 113–119.

[20] Pourmortazavi SM, Rahimi-Nasrabadi M, Khalilian-Shalamzari M, *et al*. Synthesis, structure characterization and catalytic activity of nickel tungstate nanoparticles. *Appl Surf Sci* 2012, **263**: 745–752.

[21] Fu HB, Pan CS, Zhang LW, *et al*. Synthesis, characterization and photocatalytic properties of nanosized Bi_2WO_6, $PbWO_4$ and $ZnWO_4$ catalysts. *Mater Res Bull* 2007, **42**: 696–706.

[22] Singh P, Raizada P, Pathania D, *et al*. Preparation of BSA-$ZnWO_4$ Nanocomposites with enhanced adsorptional photocatalytic activity for methylene blue degradation. *Int J Photoenergy* 2013, **2013**: 1–7.

[23] Song XC, Zheng YF, Yang E, *et al*. Photocatalytic activities of Cd-doped $ZnWO_4$ nanorods prepared by a hydrothermal process. *J Hazard Mater* 2010, **179**: 1122–1127.

[24] Casali GA. Pigmentos de TiO_2 dopado com os metais de transição Cromo e Manganês. M.Sc. Thesis. São Carlos, Brazil: Federal University of São Carlos, 2001.

[25] Park SH, Ryu JY, Choi HH, *et al*. Zinc oxide thin film doped with Al_2O_3, TiO_2 and V_2O_5 as sensitive sensor for trimethylamine gas. *Sensor Actuat B: Chem* 1998, **46**: 75–79.

[26] de Oliveira ALM, Ferreira JM, Silva MRS, *et al*. Yellow $Zn_xNi_{1-x}WO_4$ pigments obtained using a polymeric precursor method. *Dye Pigment* 2008, **77**: 210–216.

[27] Kakihana M, Yoshimura M. Synthesis and characteristics of complex multicomponent oxides prepared by polymer complex method. *Bull Chem Soc Jpn* 1999, **72**: 1427–1443.

[28] Bernardi MIB, Araújo VD, Mesquita A, *et al*. Thermal, structural and optical properties of Al_2CoO_4-crocoite composite nanoparticles used as pigments. *J Therm Anal Calorim* 2009, **97**: 923–928.

[29] Pechini MP. Method of preparing lead and alkaline earth titanates and niobates and coating method using the same to form a capacitor. U.S. Patent 3 330 697, Jul. 1967.

[30] CIE. Commission internationale de l'Eclairage proceedings, 1931. Cambridge, UK: Cambridge University Press, 1932.

[31] Quintana-Melgoza JM, Cruz-Reyes J, Avalos-Borja M. Synthesis and characterization of $NiWO_4$ crystals. *Mater Lett* 2001, **47**: 314–318.

[32] Ruiz-Fuertes J, López-Moreno S, Errandonea D, *et al*. High-pressure phase transitions and compressibility of wolframite-type tungstates. *J Appl Phys* 2010, **107**: 083506.

[33] Lever ABP, London G, McCarthy PJ. Single crystal electronic spectra of a series of trans nickel(II) complexes with N, N'-diethyl- and N, N'-dimethylethylenediamine. *Can J Chem* 1977, **55**: 3172–3189.

[34] de Oliveira ALM, Ferreira JM, Silva MRS, *et al*. Influence of the thermal treatment in the crystallization of $NiWO_4$ and $ZnWO_4$. *J Therm Anal Calorim* 2009, **97**: 167–172.

[35] Cimino A, Lo Jacono M, Schiavello M. Structural, magnetic, and optical properties of nickel oxide supported on .eta.- and .gamma.-aluminas. *J Phys Chem* 1971, **75**: 1044–1050.

[36] Bernardi MIB, Cava S, Paiva-Santos CO, *et al*. Comparison of blue pigments prepared by two different methods. *J Eur Ceram Soc* 2002, **22**: 2911–2919.

[37] Ross-Medgaarden EI, Wachs IE. Structural determination of bulk and surface tungsten oxides with UV-vis diffuse reflectance spectroscopy and Raman spectroscopy. *J Phys Chem C* 2007, **111**: 15089–15099.

[38] Kuzmin A, Kalinko A, Evarestov RA. Ab initio LCAO study of the atomic, electronic and magnetic structures and the lattice dynamics of triclinic $CuWO_4$. *Acta Mater* 2013, **61**: 371–378.

[39] Mohammadi A, Amouzegar Z, Aminzare M, *et al*. Synthesis and characterisation of $NiWO_4$ nanopowders via simple molten salt route. *Mater Res Innov* 2017, **21**: 407–412.

[40] Ovechkin AE, Ryzhikov VD, Tamulaitis G, *et al*. Luminescence of $ZnWO_4$ and $CdWO_4$ crystals. *Phys Stat Sol (a)* 1987, **103**: 285–290.

[41] Lammers MJJ, Blasse G, Robertson DS. The luminescence of cadmium tungstate ($CdWO_4$). *Phys Stat Sol (a)* 1981, **63**: 569–572.

[42] Grigorjeva L, Deych R, Millers D, *et al*. Time-resolved luminescence and absorption in $CdWO_4$. *Radiat Meas* 1998, **29**: 267–271.